Measuring Temperature and Humidity Distributions in Thermal Updrafts

Daniel Hardt
daniel@daniel-hardt.de
Technische Universität Braunschweig
Braunschweig, Germany

Ines Schaefer
ines.schaefer@uni-tuebingen.de
GUZ, Environmental Physics, University of Tübingen
Tübingen, Germany

Kai Rohde-Brandenburger
kai.rohde-brandenburger@dlr.de
Institut für Aerodynamik und Strömungstechnik, Deutsches Zentrum für Luft- und Raumfahrt e.V.
Braunschweig, Germany

Abstract

This study employs a miniaturized chilled mirror hygrometer mounted on the Discus-2c DLR research glider to measure updraft thermodynamics in the convective atmospheric boundary layer, with particular focus on the role of humidity. A flight strategy transecting thermals parallel and perpendicular to the main wind direction was chosen and 26 thermal transects were conducted over three flights. Updraft width, velocity as well as temperature, and humidity within thermals and in the surrounding air were measured. Despite large scattering, results showed an average temperature excess of $0.075\,\mathrm{K}$ in thermals. The mean relative contribution of humidity to the density difference between thermals and the surrounding air was $17.4\,\%$. This data was compared with previous studies and LES simulations. Furthermore, the horizontal fine structure of humidity and temperature in and around thermals displayed non-uniform characteristics in wind direction and perpendicular to the wind direction.

Nomenclature

$\Delta(\cdot)$	difference
$\overline{(\cdot)}$	mean
$(\cdot)_T$	thermal
$(\cdot)_A$	thermal surrounding
d	diameter [m]
f	frequency [Hz]
M_L	molar mass of dry air [$\mathrm{kg\,mol^{-1}}$]
M_v	molar mass of moist air [$\mathrm{kg\,mol^{-1}}$]
M_W	molar mass of water vapor [$\mathrm{kg\,mol^{-1}}$]
p_{ref}	reference pressure [Pa]
p_s	static air pressure [Pa]
p_t	total air pressure [Pa]
q	specific humidity [$\mathrm{g\,kg^{-1}}$]
r	mixing ratio [$\mathrm{g\,kg^{-1}}$]
r_T	recovery factor [-]
R	universal gas constant [$\mathrm{J\,K^{-1}\,mol^{-1}}$]
T	static temperature [K]
T_m	measured temperature [K]
T_t	total temperature [K]
T_v	virtual temperature [K]
v	flight velocity [$\mathrm{m\,s^{-1}}$]
w	updraft velocity [$\mathrm{m\,s^{-1}}$]
$\overline{w}_T$	mean updraft velocity [$\mathrm{m\,s^{-1}}$]
$w_{\mathrm{max},T}$	maximum updraft velocity [$\mathrm{m\,s^{-1}}$]

This article was peer reviewed by two independent, anonymous reviewers.

z	height [m]
z_i	convective boundary layer height [m]
z_*	dimensionless height [$-$]
κ_L	heat capacity ratio of dry air [-]
κ_v	heat capacity ratio of moist air [-]
Θ	potential temperature [K]
Θ_v	virtual potential temperature [K]
ϑ_d	dew point temperature [°C]
ρ_L	density of dry air [$\mathrm{kg\,m^{-3}}$]
ρ_v	density of moist air [$\mathrm{kg\,m^{-3}}$]
ρ_W	density of water vapor [$\mathrm{kg\,m^{-3}}$]
$\sigma_{w,T}$	standard deviation of the updraft velocity [$\mathrm{m\,s^{-1}}$]

Introduction

Thermals are turbulent features in the convective boundary layer (CBL). In atmospheric science, they are often described using statistical properties considering sufficiently long time and length scales. In gliding, however, thermals are commonly conceptualized as distinct events. Here, the atmospheric boundary layer may be assumed to be a shallow convection Boussinesq regime where a buoyancy flux of latent and sensible heat from the earth's surface causes convection. The vertical acceleration of an air parcel then depends on its buoyancy, the vertical pressure gradient force and viscous effects. To measure the buoyancy of an updraft, its density needs to be determined relative to the surrounding air. Hence, an atmospheric dataset including vertical velocity, temperature and humidity needs to be available at sufficiently high spatial resolution. There are some approaches to characterizing single updrafts using ground or airplane based remote sensing techniques, such as the differential absorption Lidar (DIAL) reaching spatial resolutions of several 10 m in the case of ground-based systems [1] and $\sim$150 m depending on airspeed for airborne measurements [2]. In-situ plane-based measurements have been used to investigate the properties of the CBL in the past at higher resolution [3, 4].

However, aircraft-based meteorological studies on thermals often aim at improving the understanding of vertical transport processes and weather modeling. They often overlook specifics influencing single updraft characteristics relevant for glider pilots. A cost-effective and reliable methodology for independent research can help establish a data base for research on these problems. In-situ measurements to determine the characteristics of an updraft compared to its surrounding requires horizontal fly-trough maneuvers as demonstrated by Williams and Hacker [5] and Lenschow [6]. At a typical reference airspeed of a glider of 100 km/h (28 m/s), and an updraft diameter of several hundred meters up to kilometers [7], a thermal transect would take approximately 15 s to 30 s. This effectively sets the benchmark of the temporal resolution to several samples per second in order to resolve the fine structure of a thermal updraft as shown by Williams and Hacker [5]. While data on the vertical wind component is abundantly available at a sufficient resolution through compensated lift indicators as well as flight state estimates aided by inertial navigation systems, e.g. Pätzold [8], an accurate air density measurement requires data on the static pressure, temperature and water vapor content, necessitating more specialized equipment.

The measurement resolution is typically limited by the humidity sensor. Sensors using a capacity-based measurement principle rely on molecular diffusion of water vapor into the sensor cavity. These sensors such as the Bosch BME380, which have been used in glider measurements in the past [9, 10], have typical response times longer than 5 seconds which would not be sufficient for resolving the thermodynamics of a thermal updraft in a fly-trough. Furthermore, the derived air densities can be biased to a phase-shifted response of the humidity and temperature sensors. Sonntag et al. [11] give an overview over various humidity sensors. They do not classify any capacity-based sensors response time to be fast enough for turbulence measurements. Meteorological field experiments investigating the atmospheric boundary layer often rely on spectral instruments such as the Lyman-α or Licor gas analyzer [12]. Such instruments, however, are difficult to integrate into smaller aircraft due to cost and weight limitations. Mauz et al. [13] have developed a miniaturized chilled mirror hygrometer (CMH) that achieves a temporal resolution of several Hz and qualifies for integration in small aircraft such as uncrewed aerial systems (UAS) or gliders. A CMH measures the dew point of an air mass directly by cooling a mirror surface to the point where condensation occurs [11]. Condensation is optically detected by measuring the mirror surfaces reflectivity, scattering or both within the near-infrared spectrum. The high measurement resolution of the design by Mauz et al. [13] is achieved by minimizing the size and therefore thermal inertia of the sensor unit and a PID-controlled cooling system.

This investigation presents an approach to sample several characteristic quantities of thermal updrafts with particular focus on the water vapor content using a glider. A CMH prototype provided by the University of Tübingen has been integrated into a newly developed sensor pod outside the fuselage under the right wing of the research glider Discus-2c DLR. Twenty-six (26) transects through thermal updrafts have been conducted in this configuration.

Methods

Humidity, Temperature and Density Measures in the Atmospheric Boundary Layer

The density of air in the lower atmosphere depends on the static pressure, temperature and humidity. It is calculated as

$$\rho_v = \frac{M_v p_s}{RT}, \tag{1}$$

where R is the universal gas constant and M_v the molar mass of moist air. To better compare the densities of air parcels of different temperature and humidity, the virtual temperature T_v is commonly used. The virtual temperature is the temperature of a

dry air parcel with the same density as a moist air parcel at the same pressure. Therefore, the density is given by

$$\rho_v = \frac{M_L p_s}{R T_v}, \tag{2}$$

where M_L is the molar mass of dry air. The virtual temperature is given by Stull [14, cfr. appendix D],

$$T_v = T\left[1 + \left(\frac{1-\frac{M_W}{M_L}}{\frac{M_W}{M_L}}\right) r\right] \approx T\left(1 + 0.61 r\right). \tag{3}$$

Here, the measure of the water vapor content is the mixing ratio $r = \frac{\rho_W}{\rho_L}$, where ρ_L is the density of the dry air and ρ_W is the density of the water vapor in an air parcel. The water vapor content can also be expressed as the specific humidity $q = \frac{\rho_W}{\rho_W + \rho_L}$. M_W is the molar mass of water vapor. A detailed overview on different measures of water vapor in the atmosphere is given by Stull [15].

If temperature is measured in moving air, the flow is decelerated at the temperature sensor. The resulting conversion of part of the kinetic energy of the flow into heat is called adiabatic heating. Therefore, the static temperature of the air T is calculated from the measured temperature T_m as follows [16, 17]:

$$T = T_m r_T \left(\frac{p_s}{p_t}\right)^{\kappa_v}, \tag{4}$$

where p_t and p_s are the total and static pressure of the air, κ_v is the heat capacity ratio of moist air and r_T the recovery factor. The recovery factor is a measure of the degree of deceleration and lies between zero and one.

To compare the temperature of air parcels at different pressure levels, the potential temperature can be used. The potential temperature is the temperature an air parcel would have if it were transported adiabatically to a reference pressure level (usually $p_{\text{ref}} = 1000\,\text{hPa}$). The potential temperature is calculated from the static temperature and the static pressure as

$$\Theta = T\left(\frac{p_{\text{ref}}}{p_s}\right)^{\frac{\kappa_v - 1}{\kappa_v}}. \tag{5}$$

To compare the virtual temperatures at different altitudes, i.e. different pressure levels, the virtual potential temperature can be calculated from the virtual temperature,

$$\Theta_v = T_v\left(\frac{p_{\text{ref}}}{p_s}\right)^{\frac{\kappa_L - 1}{\kappa_L}}, \tag{6}$$

where κ_L is the heat capacity ratio of dry air, which is 1.4. The virtual potential temperature thus corresponds to the temperature of an air parcel of dry air at the reference pressure level with the same density as the humid air parcel. Therefore, it is an altitude-independent measure of the density of a moist air parcel. With Θ_v, the density of moist air is calculated as

$$\rho_v = \frac{M_L p_{\text{ref}}}{R \Theta_v}. \tag{7}$$

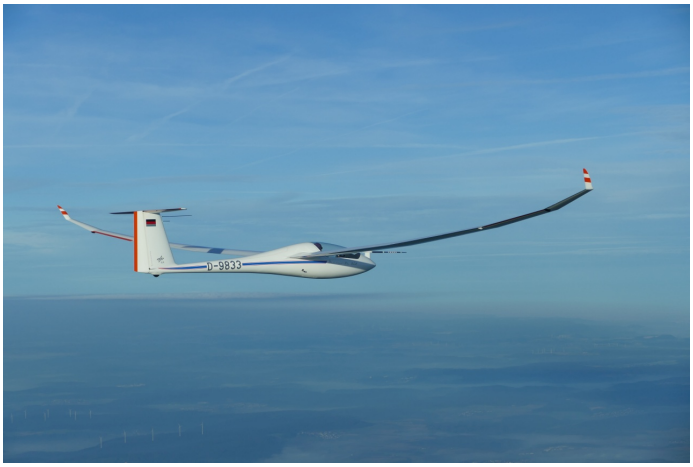
The meteorological calculations described above are carried out using the Python package `parmesan` [18].

Thermals are a central feature of the convective boundary layer. They develop as a result of an instability created by the buoyancy flux at earth's surface. The boundary layer can be divided into an inner layer, consisting of the roughness sub-layer and the inertial sub-layer, and an outer layer [19, chapter 3]. While thermals originate in the inner layer, where surface inhomogeneity and increasing wind speed with height strongly influence atmospheric dynamics, they are of primary interest to glider pilots in the outer layer. The outer layer is also called the mixed layer (ML) where the mean wind and specific humidity are constant and the temperature profile follows the adiabatic temperature gradient. This means that the potential temperature and mixing ratio are on average constant over height. In favorable soaring conditions, the ML is typically capped by a stable layer (increase of virtual potential temperature with increasing height) acting as an effective limit for the vertical air movement. At the boundary between the CBL and the free atmosphere (FA) lies the entrainment zone where drier air of higher potential temperature is mixed into the CBL. Hunt [20] provides a more detailed overview of the kinematics of individual thermals as well mixing effects with the surrounding air mass. Williams and Hacker [21] developed a conceptual model of surface-layer dynamics, focusing on how plumes and thermals interact across the boundary between the surface and mixed layer. They describe how surface-layer plumes organize, feeding the large-scale convective motions that dominate the mixed layer.

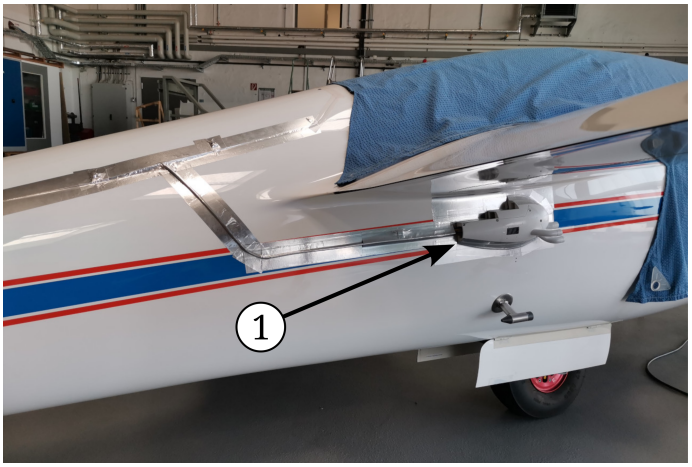
Measurement System and Strategy

Flight measurements were conducted aboard the research glider Discus-2c DLR of the German Aerospace Center (Deutsche Zentrum für Luft- und Raumfahrt e.V. - DLR) (see Fig. 1a). The Discus-2c DLR is based on the Discus-2c series glider manufactured by Schempp-Hirth. The aircraft has a wingspan of 18 m and a maximum take-off mass of 565 kg. It is equipped with an extensive sensor system to measure the flight state and atmospheric flow at high precision. A detailed description of the Discus-2c DLR and its sensor system can be found in Raab and Rohde-Brandenburger [22].

The Discus-2c DLR sensor system has been augmented with a sensor pod housing a fast response temperature and humidity measurement unit located at the fuselage under the right wing. The unit is called the Fast-response Temperature and Humidity sensor Pod (FTHP). Its main component is a CMH using the design by Mauz et al. [13]. The temperature of the air stream and the mirror surface of the CMH are measured by Type T thermocouples of 76 µm diameter. The airflow arrangement through the FTHP consists of three separate ducts for the measured air and the cooling air for the CMH and the electronics whose inlets are designed to protrude from the boundary layer of the fuselage. In addition, a Sensirion SHT31 capacitive temperature and humidity sensor is integrated into the measuring system. This sensor has a relative accuracy of $\pm 2\,\%$ and a response time of 8 s [23],



(a) Discus-2c DLR in flight.



(b) Integration of the FTHP.

Fig. 1: Research aircraft Discus-2c DLR with the FTHP (1) attached to the right side of the fuselage.

which is typical for sensors using a capacity-based measurement principle. Data from the FTHP were sampled at a frequency of 50 Hz, all other flight state variables were sampled at 20 Hz.

The recovery factor r_T for the conversion from measured temperature to static temperature is assumed to be one. This assumption is deemed acceptable given that the measurement sections are flown at a constant airspeed and the focus is on temperature differences. The order of magnitude of the adiabatic heating at an airspeed of 100 km/h is 0.4 K.

The vertical wind component was not calculated explicitly because, at the time of the measurements, the required Inertial Measurement Unit (IMU) velocities could not be recorded. Therefore, it was calculated from the sink rate of the glider, compensated for total energy as well as using the well-established flight performance data of the Discus-2c DLR [24]. The sink rate was logged by the LX9000 variometer with a resolution of 1 Hz. For the FTHP, calibration experiments have been conducted in the laboratory as well as in validation flights.

A static calibration of the FTHP was performed in the climate chamber at the Institute of Aerodynamics and Flow Technology of the DLR (climate chamber model: "SkyEvent TA-TAH" by Weiss Technik). The FTHP was ventilated by the climate chambers fan during the calibration measurements. The calibration was performed at temperatures of 10 °C, 20 °C and 30 °C and relative humidity levels of 20 %, 40 %, 60 %, 80 % and 95 %. The results are used for an offset correction in two dimensions (temperature and dew point). After applying the linear correction factors obtained in the climate chamber calibration, the standard deviation of the calibration data is 0.10 K for the air temperature thermocouple and 0.24 K for the dew point of the CMH.

A pseudo-step function was generated in the climate chamber. The relative humidity and subsequently the dew point in the chamber changed rapidly due to water vapor injection into the chamber. The sensor responses to the pseudo-step from a relative humidity of 40 % to 60 % are displayed in Fig. 2 and provide some indication of the inertia of the capacitive SHT31 sensor and the CMH. In the static setting before the step between 0 s to 45 s, the dew point measured by the CMH oscillated slightly stronger than the one measured by the SHT31 in the range of 0.1 K. When performing the step, there was a delay in the step response of approximately 5 s to 10 s for the SHT31. The CMH reacted considerably faster to the changing environment of the climate chamber. After the step, both sensors show an oscillation around the new dew point which indicates a control oscillation of the climate chamber.

In flight tests the FTHP was examined regarding effects of the flight state on the measurement results. To investigate how flight conditions influence the measurement of temperature and humidity, a number of test points were performed in low turbulence conditions. Two factors were investigated:

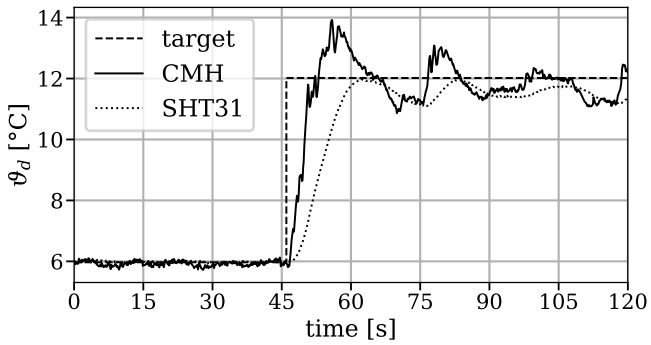


Fig. 2: Response of the sensors to a pseudo-step in the target value of the relative humidity of the climate chamber from 40 % to 60 % at 20 °C (calibrated sensor data). Oscillations around the new target temperature can be attributed to the climate chamber control and water injection system.

- Influence of airspeed/angle of attack: measurement sections of 20 s each with an indicated airspeed (IAS) of 80 km/h, 100 km/h, 150 km/h and 200 km/h.
- Influence of sideslip: four measurement sections with 10° and 20° sideslip to the left and right at 100 km/h IAS.

The temperature and the humidity sensors within the FTHP showed a slight dependence on the airspeed and the angle of sideslip for air speeds greater than 150 km/h IAS and sideslip angles of more than 10°. However, this dependency has no significant influence on the measurement of the horizontal thermal cross-sections, since these measurement sections are flown at constant airspeed and with negligible sideslip angle.

The temporal resolution of the system in flight was investigated using spectral analysis of the airborne data. Assuming Taylor's frozen-turbulence hypothesis [3], since the aircraft's airspeed greatly exceeds the ambient wind speed, the airborne measurements should exhibit Kolmogorov inertial-subrange scaling, with power spectral density proportional to $k^{-5/3}$ with k as the wavenumber in the inertial sub-range.

This method has been applied by Mauz et al. [13] and Greiner and Würz [25] in case of the wind speed. The power spectral density is expected to be either dominated by sensor noise or system inertia where it stops to follow $k^{-5/3}$ around the maximum measurement frequency. The inertial sub-range is expected to extend into the sub-millimeter range, where viscous effects dominate which is well above the sensor resolution. Straight flight intervals were selected in the CBL to analyze the power spectral density of temperature and dew point data. A mean spectrum was calculated from all intervals.

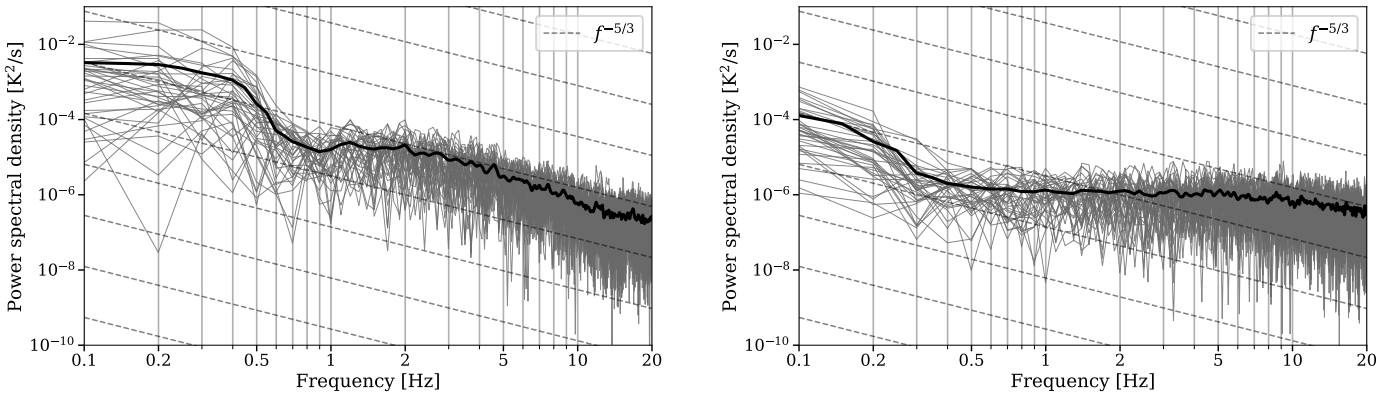
The humidity power spectra from straight flight measurement sections displayed in Fig. 3 show a decline of the humidity signal with increasing frequency. The CMH dew point resembles the expected Kolmogorov eddy decay. However, there is a dent in the distribution at 0.5 Hz to 1 Hz and a slightly decreased slope between 1 Hz and 5 Hz deviating from ideal eddy decay for free turbulence. Sensor noise can be identified at frequencies slightly above 10 Hz. Contrarily, there is no Kolmogorov eddy-decay signature visible in the SHT31 signal indicating that turbulent eddies cannot be resolved and that the sensor resolution is at least above 5 s. Cross-correlation of the different humidity measurements using in-flight data (excluding the air tow) yields a 5 s lag in case of the SHT31 sensor.

An additional plausibility check was performed analyzing vertical profiles of potential and virtual potential temperature to assess their conformity with atmospheric boundary layer models, as detailed in sources such as [15] and [19]. Figure 4 shows the measured profiles of the potential temperature and virtual potential temperature over height of flight 1 (04.08.2022 between 14:34 and 17:21 LT at Brunswick). The inversion height was estimated at approximately 3000 m from the radiosonde measurement of the Lindenberg Meteorological Observatory - Richard Aßmann-Observatory (MOL-RAO) of the German Meteorological Service (DWD) for this flight due to airspace restrictions. The potential temperature profile does not show a trend with altitude. This is typical for the well-mixed fully developed convective boundary layer [15, chapter 8]. Fluctuations are in the range of 1 K. Thermal updrafts indicated by colored points show similar variation of the potential temperature as non-thermalling sections. The virtual potential temperature of the same measurement shows similar variation and no trend above approximately 1000 m height. Below the level of 1000 m, Θ_v decreases with height indicating latent instability through humidity injected into the atmosphere from the ground. Θ_v is approximately 1.5 K higher than Θ in the well-mixed layer. Overall, the vertical profiles are in agreement with conventional meteorological models of the CBL.

The cross-sections of single updrafts were measured at several altitudes between the cloud base and 500 m above ground level (AGL) with 100 km/h IAS. The height and lapse rate of the CBL is measured by towing the glider above the cloud base to record a vertical profile. After centering the updraft, cross-sections of thermals and the surrounding air were performed parallel and perpendicular to the main wind direction (see Fig. 5). The flight path was adjusted in relation to the cumulus cloud generated by the updraft. Measurement sections where the updraft was missed were discarded.

Updrafts are classified as the zone in which the vertical wind velocity is positive over a sustained period and align with cloud features and the experience of the pilot. $z_* = \frac{z}{z_i}$ is used as normalized height level when comparing updraft properties over the height, where z is the mean height of the transect through the thermal and z_i is the convective boundary layer height. When comparing updrafts in the horizontal cross-sections, the distance along the straight flight section through the updraft (TAS integrated over time) was normalized to $[-1, 1]$. For each measurement section as well as the updraft sections, the mean values of potential temperature, virtual potential temperature and specific humidity were calculated and subsequently subtracted to evaluate the differences between updrafts and the surrounding air. The difference $\Delta\Theta_v$ between updraft and surrounding air is used as a measure for the density of the updraft compared its surrounding. The potential temperature difference $\Delta\Theta$ neglects the effect of humidity. The contribution of humidity to the density difference of the updraft to its surrounding is calculated as $(\Delta\Theta_v - \Delta\Theta)/\Delta\Theta_v$.

An example of an updraft measurement is given in Fig. 6. During the glider's approach to the thermal, the glider sinks approximately 50 m over a distance of 3 km. The true airspeed is kept within a range of approximately $\pm$ 7 km/h. The vertical wind velocity signal is rather irregular which leads to some ambiguity in the segmentation methodology. The peak updraft velocity of 2 m/s is reached in the last third of the pass-through towards the windward side of the updraft (Fig. 6, gray region). The updraft shows a slight increase in Θ as well as Θ_v in the order of 0.2 K reaching a maximum in the last third of the pass-though whereas the temperature maximum extends into the sinking air around the thermal. Comparison of the SHT31 sensor with the



(a) CMH. (b) SHT.

Fig. 3: Dew point power spectra of the CMH and SHT measurements for 10 s segments of straight flight near the entrainment zone as well as the average spectra over those segments.

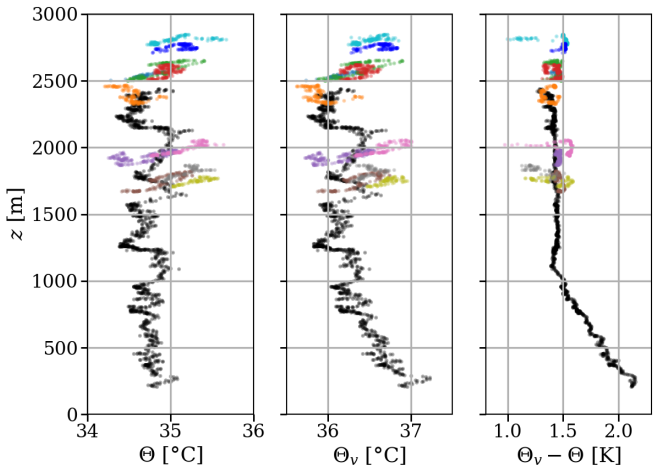


Fig. 4: Measured profiles of the potential temperature and virtual potential temperature of flight 1 (14:34 - 17:21 LT) and the difference between potential and virtual potential temperature to illustrate the contribution of humidity. Only the aerotow and straight measurement sections are shown. The aerotow is shown dotted in black and the measurement sections are color dotted.

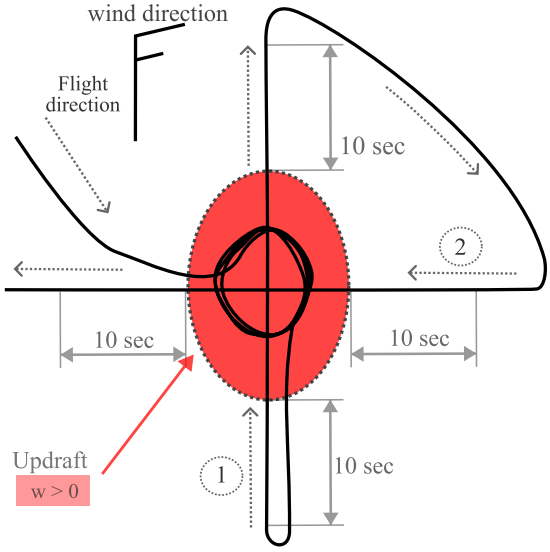


Fig. 5: Flight strategy for measuring thermal cross-section at one altitude (top view of a horizontal slice through the thermal). 1: headwind section, 2: crosswind section.

CMH shows an overall similar signal with an offset of approximately 0.2 K and a low-pass response characteristic with a phase shift similar to that observed in the calibration experiments. The cooling power needed to maintain the target illumination value is between 15 and 32 % reacting to changes in measured illuminance. The stability of cooling power and illuminance indicate that the CMH control loop was adequately tuned for the measurement regimen whereas the illuminance stayed within 2 % of the target value.

The measured data was compared with the results from Milford [26] and Maas and Etling [27]. Maas and Etling performed simulations with different values for the Bowen ratio, the ratio of surface sensible to latent heat flux [28], and the humidity difference from the ML to the FA using the PALM large eddy model [29] with a model domain of 8.2 km x 5.1 km x 3.3 km at a horizontal resolution of 32 m.

Results

In August 2022, three measurement flights were conducted in central Germany (see Appendix and Table 1). Sensor tuning was improved after flight 2; flight 3 was performed with a Duo Discus XL and a slightly modified setup where the airspeed and updraft velocity were derived from an LX9000 variometer log (resolution: 1 Hz). In all flights, updraft cross-sections were car-

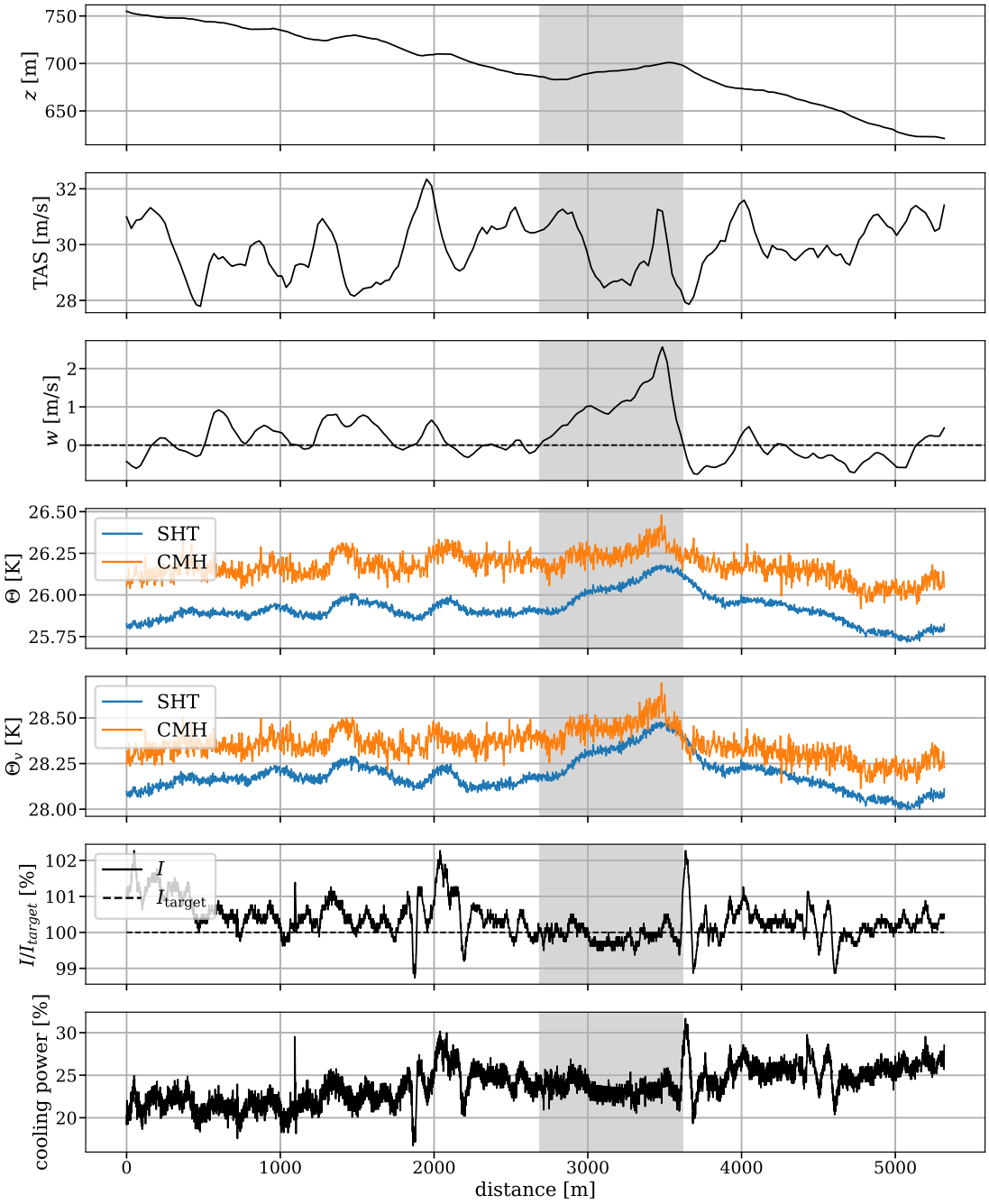


Fig. 6: Representative data log of a straight flight segment containing an headwind thermal pass-through of flight 3. The segment classified as updraft is marked in grey. I/I_{target} represents the measured illuminance relative to the target illuminance, which corresponds to the deviation of the control loop.

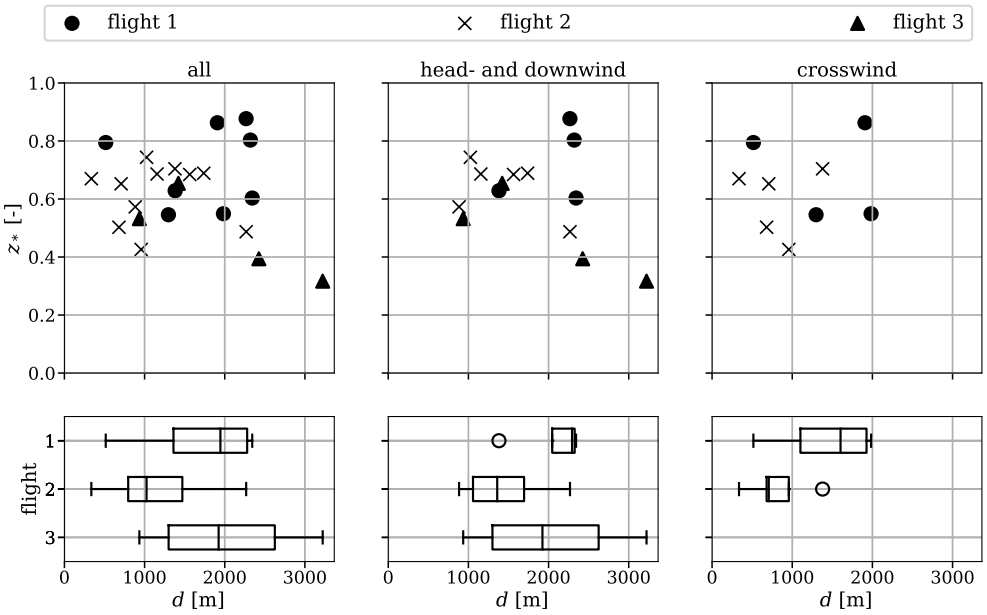


Fig. 7: Horizontal extent of the updrafts above the dimensionless height, for all measurement sections and grouped by measurement sections parallel and perpendicular to the main wind direction. The distribution of the data grouped by flight is shown as boxplots. The boxplots contain the following statistical data: *Median*: line in box; *Interquartile range*: box; *1.5 times the interquartile range*: "Antennae"; *Outliers*: points.

ried out in a height of 500 m to 2800 m AGL, or 40 % to 90 % of the height of the CBL.

The horizontal extent of the updrafts varied between 500 m and 2500 m, which corresponds to $d = (0.4 \ldots 1.0) \cdot z_i$ (Fig. 7). The measured updraft width is larger than in other studies [30–32]. Almost all other models and measurements that were reviewed assumed smaller updrafts than the measured ones. Carmichel [33] found updraft diameters of 200 m to 600 m. In the measurements of Milford [26] and Ultsch [34], diameters of 250 m to 550 m and 500 m were measured, respectively. Konovalov [7, fig. 2] gives the frequency distribution of the updraft diameters that range from 250 m to 1700 m. The diameters presented in Kubrynski [35] of 400 m to 2000 m agree with our measurements. Stull [14, p. 461] describes larger updraft diameters of $1.5 \cdot z_i$ than found in this study. Furthermore, updrafts were not circular, but their horizontal extent in the main wind direction was on average approximately twice as large as perpendicular to the main wind direction. The quotient of measured updraft width in the main wind direction to the width perpendicular to the main wind was in the same range as observed by Träumner et al. [36] ("anisotropy factor" of 2 to 3). The updraft width exhibit considerable variability and no significant trend of updraft width with height was measured.

Like the width of the updrafts, updraft velocities were also scattered widely and were only measured in the upper part of the CBL, so no statement can be made about the course of the updraft velocity over normalized height (Fig. 8). The mean updraft velocity of the thermals was in the range of about 1 m/s to 3 m/s, the maximum updraft velocity of 2 m/s to 7 m/s and the standard deviation of updraft velocity in the thermals of 0.5 m/s to 2 m/s. There was no significant difference whether the measurement sections were parallel or perpendicular to the mean horizontal wind. The updraft velocities of most other models and measurements (Horstmann [37], Rohde-Brandenburger [24], Ronig [38], Ultsch [34], Kubrynski [35], Carmichel [33], and Lindemann [39]) agree well with our measurements. Only the maximum updraft velocities by Konovalov [7, fig. 3] are smaller than our measurements.

The deviation of the virtual potential temperature Θ_v in the updraft (index T) from the measurement section mean (index A) is diagrammed on the left side of Fig. 9. On average, the difference of the virtual potential temperature between a thermal updraft and the surrounding air is 0.091 K, the difference of the potential temperature is 0.075 K. The measured temperature differences show no dependency on z_* and are of the same order of magnitude as those measured by Milford [26], and those calculated by Maas and Etling [27] for the simulations with the Bowen ratio of one. Milford [40] and Lindemann [41] also measured temperature differences of 0.5 K in about 200 m AGL, which decrease to 0 K to 0.1 K with increasing height.

The humidity differences measured, as shown in Fig. 9, right panel, are relatively small compared to the simulations in Maas and Etling [27]. The simulation with a Bowen ratio of one and no humidity difference between the ML and the FA agrees best with the measured values. Lindemann [39] also measured specific humidity differences on the order of 0.3 g/kg; Milford [40]

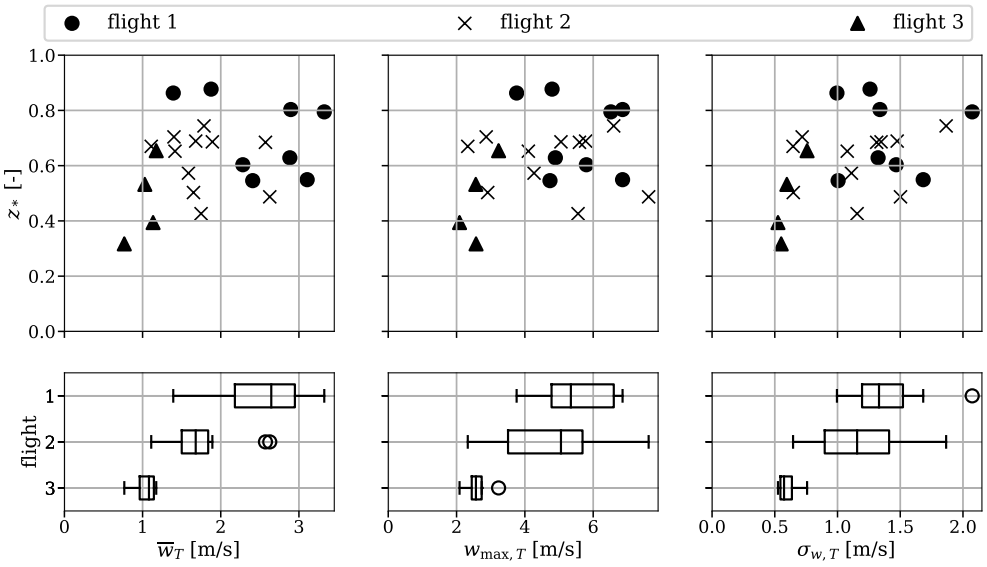


Fig. 8: Mean and maximum updraft velocity, as well as standard deviation of the updraft velocity of the updrafts over the dimensionless height for all measurement sections. The boxplots adhere to the same layout as described in Fig. 7.

measured deviations in specific humidity of about $\pm 0.5\,\mathrm{g/kg}$. For most of the measurement sections, the updraft was more humid than the surroundings (on average $0.086\,\mathrm{g/kg}$). The contribution of humidity to the density difference between the updraft and its surroundings, averaged over all measurement sections, is $17.4\,\%$. There are differences between the three flight datasets that were recorded in different weather situations during good gliding conditions. In the dataset presented, more humidity in the updrafts compared to the surroundings is linked to wider updrafts and faster upward velocity. Notably, some updrafts were drier than their surroundings, and some even had a lower virtual potential temperature and thus a greater density than their surroundings.

Figure 10 presents the updraft velocity along the horizontal cross sections, averaged over the headwind and crosswind sections. Before averaging, the updraft velocity was normalized with the mean updraft velocity. With this normalization strong updrafts are not weighted more than weak ones while averaging. The horizontal distance along the flight section through the updraft was normalized to $[-1, 1]$ as described in the "Methods" section. The averaged courses, or profiles, show a clearly defined updraft core with an updraft velocity varying around a constant baseline.

The horizontal cross-section temperature and humidity show an asymmetric characteristic with a sharper jump in humidity on the windward side of the updraft than on the leeward side or the crosswind sections (Figs. 11 and 12). The potential temperature maximum is located on the windward side of the updraft. Asymmetric distributions of heat flux have also been found by Williams and Hacker [5].

Discussion

A miniaturized chilled mirror hygrometer has been integrated into a research glider and first measurements of thermals in the upper half of the convective boundary layer have been conducted.

Laboratory data indicate that the CMH is suitable for measuring the humidity of thermals in terms of accuracy and response time. A direct comparison with the CMH illustrates the inertia of state-of-the-art low-cost capacity-based sensors to detect small changes in humidity. These sensors are not fast enough for airborne measurements of turbulent phenomena. Flight tests of the integrated setup showed the sensitivity of the sensor setup to altered flow around the fuselage as found for side-slip maneuvers and airspeed variations. These effects must be mitigated by the flight strategy which relies on constant airspeed, straight flight, and negligible angles of sideslip. The flight state variables can be precisely measured aboard the research aircraft. This means that sufficient quality assurance can be put in place to avoid biased data due to inaccurate flight maneuvers by checking flight state data during analysis. The flight strategy presented using systematic fly-though maneuvers produced air data in the direct vicinity of the thermal, which can be regarded as an approximate height level reference. This flight strategy is more consistent with the strategies of flight experiments in boundary layer research than glider-based measurements taken during regular cross-country flights. Nevertheless, this strategy does not deliver reference at a constant height due to the limitations of a non-motorized glider. Flight tests were used to confirm the resolution estimates of the humidity measurement with the power spectral density resembling the $k^{-5/3}$ Kolmogorov eddy decay footprint of a free turbulence regime between 1 Hz and 10 Hz

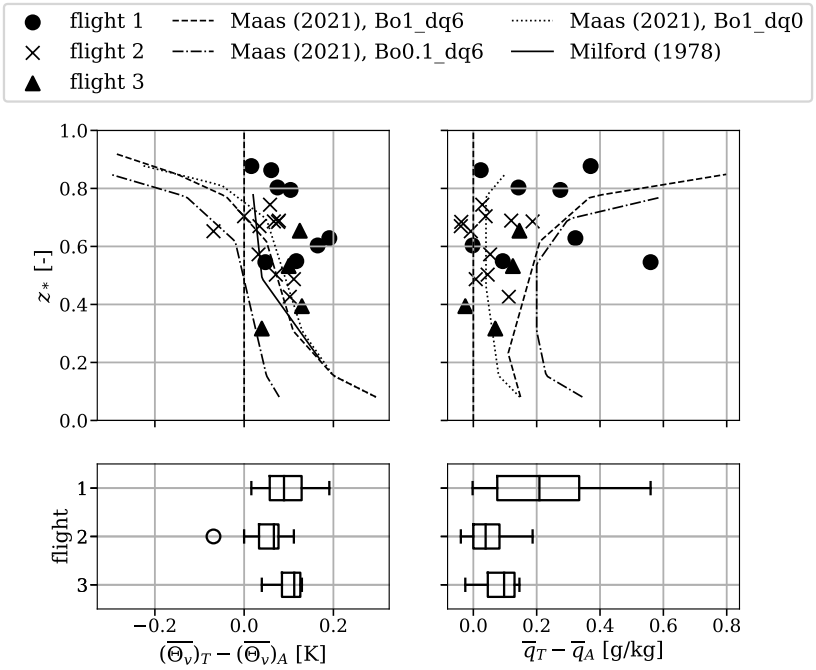
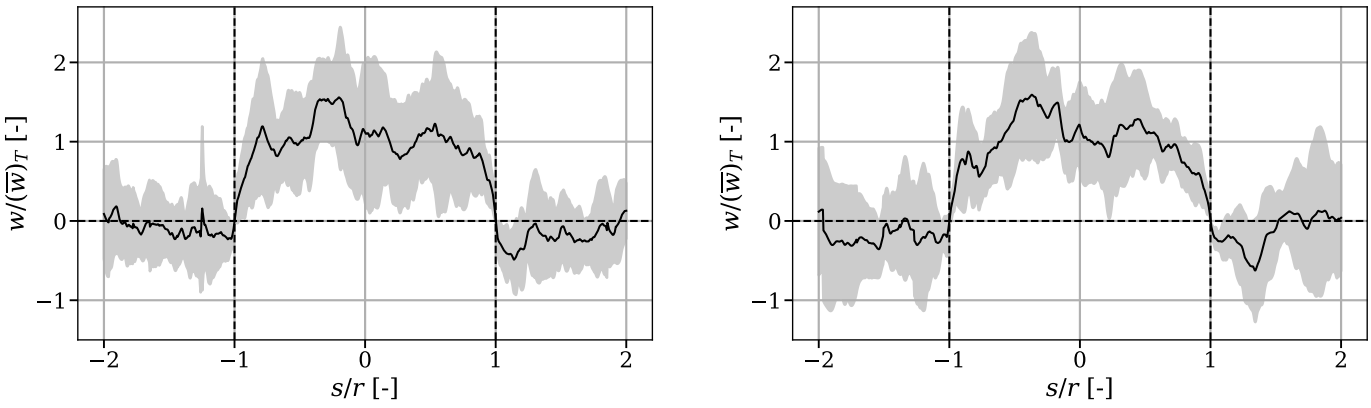


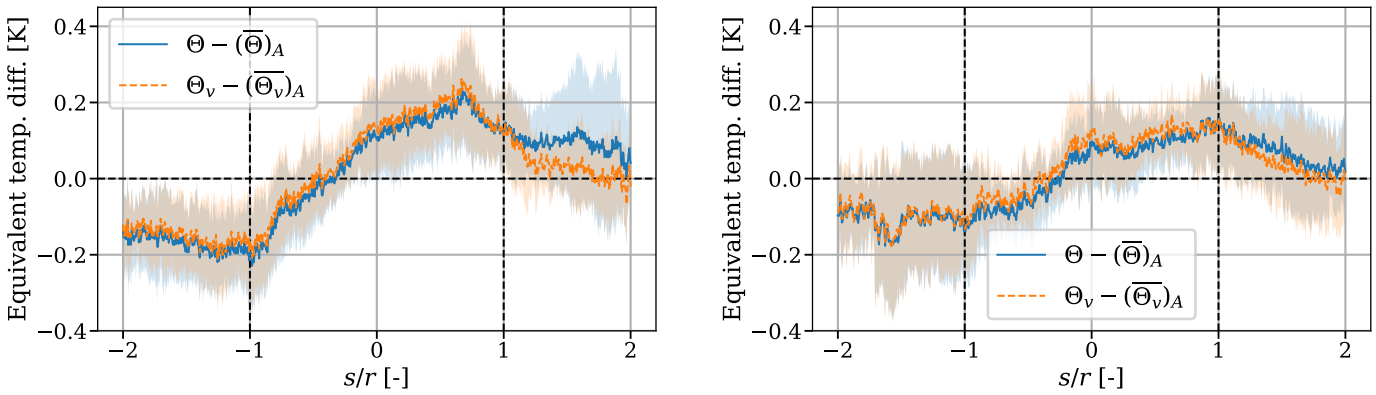
Fig. 9: Difference of the mean virtual potential temperature (measure of density difference, left) and the specific humidity (right) of the updraft to the mean temperature or specific humidity of the measurement section. The lines represent profiles of data available in [26,27]. The boxplot layout is the same as in Fig. 7.



(a) Headwind sections.

(b) Crosswind sections.

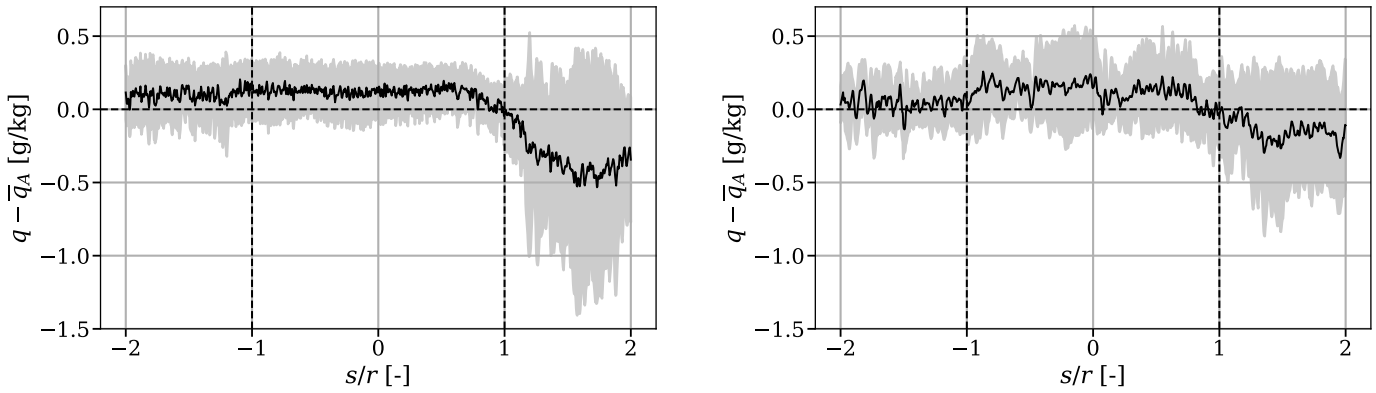
Fig. 10: Averaged courses, or profiles, of updraft velocity over the horizontal normalized distance. The updraft velocity is shown normalized with the mean updraft velocity. The shaded area is the standard deviation of the averaged curve.



(a) Headwind sections.

(b) Crosswind sections.

Fig. 11: Averaged potential and virtual potential temperature over the horizontal normalized distance. The shaded areas mark the standard deviation of the averaged curves.



(a) Headwind sections.

(b) Crosswind sections.

Fig. 12: Averaged specific humidity over the horizontal normalized distance. The shaded area is the standard deviation of the averaged curve.

reproducing the results from Mauz et al. [13]. The deviation from the ideal $k^{-5/3}$ relationship at resolutions lower than 1 Hz is unclear but has been measured by Mauz et al. [13] in a similar way. In addition, the turbulence characteristics within the entrainment zone could differ from the presumed free turbulence regime.

The measured temperature profiles over height (see Fig. 4 for flight 1) indicate a fully developed ML, which is to be expected for the weather conditions of the measurement flights. The temperature variability on the order of 1 K is comparatively small and in the expected range for a CBL. Despite the considerable spatial and temporal differences between the radiosonde and glider measurement locations a similar meteorological situation was observed regarding boundary layer height, stratification and temperature. The measurements from the glider in the afternoon exhibit a closer correlation with the atmospheric conditions indicated in the 20:00 LT radiosonde sounding, as opposed to the 14:00 LT sounding. Possibly the ML had reached a state close to equilibrium in the late afternoon. The measurements also showed that thermals generally contained a section that was several tenths of Kelvin warmer than the surrounding atmosphere.

The flight test results in combination with the laboratory experiments show that it is possible to derive meaningful atmospheric data using the sensor unit with the described pass-through flight strategy. The vertical profile further suggests that a typical cross-country flight strategy where a thermal is entered and left at significantly different altitudes is prone to errors due to the spatio-temporal variance of the atmospheric boundary layer. In addition, the spatial extent of updrafts investigated using the pass-through maneuvers tended to be larger than the circling diameter in thermalling.

The characteristics of the updrafts were analyzed with respect to height. All 26 measurements were carried out exclusively in the upper half of the CBL. The velocity scale of the updrafts was similar to other studies [30–32]. However, there is little information on factors that can influence the updraft size such as terrain, surface heat flux, mean wind or boundary layer height. These factors make a more detailed analysis unfeasible. Measured differences in Θ and Θ_v between the updrafts and their surrounding were in the range of few tenths of Kelvin, and generally agree with meteorological literature [5, 6, 27, 39]. For all variables investigated, no significant altitude dependence was detected. This result is partly caused by the relatively large scattering of the data combined with the small sample size. Another potential bias is the identification of thermals by their vertical velocity. Maas and Etling [27] include the Deardorff scaling velocity (buoyancy velocity scale for the convective mixed layer derived using similarity theory, cfr. [14, 42]) as a lower bound to identify updrafts for further analysis. Studies with motor aircraft or modeling studies typically use a larger scale level average, typically based on measurement sections longer than 10 km, as a reference instead of the direct surrounding of the thermals. The measured temperature excess compared to a thermal's surrounding is larger than in Maas and Etling [27] whereas the humidity excess is smaller. The excess temperature and humidity is maintained well into the highest part of the CBL where entrainment of warmer, drier air from the FA is expected to increase the humidity excess and reduce the temperature excess. Condensation was not included in the model setup used by Maas and Etling [27] whereas all our measurements were conducted in cumulus cloud conditions.

The average updraft vertical velocity course in the updraft tended to have a trapezoidal shape: over most of the updraft, the vertical velocity was almost constant, at the edges the vertical velocity increased or decreased steeply. This result, however, did not occur in each individual thermal. Konovalov [7] measured this behavior too and named it "type a" thermals.

Despite the dataset suffering from little statistical significance due to the small number of measurements, several features were derived from the mean data of the thermal cross sections. The updraft velocity plateau had a tendency to exhibit a slightly reduced updraft velocity in the center of the thermal. This effect was also measured by Childress [31] and linked to a phenomenon referred as "Convection Cells" (merging of multiple updrafts with increasing height). When analyzing the individual measurement sections, an updraft velocity course with two maxima was found in almost half of the measurement sections (Childress [31] found these in 60 % of the updrafts). Williams and Hacker [5] also describe an indentation feature in the center of the thermal in updraft velocity, temperature and humidity.

Several other features of the horizontal cross-sections were found in Williams and Hacker [5]. They found a similar asymmetry in the potential temperature as well as the buoyancy flux courses with a sharper edge on the windward side. Williams and Hacker [5] suggest that the temperature within thermals tends to become more uniform as it reaches half the CBL height. However, this effect could be a result of asymmetric temperature distributions lower in the thermal developing during the warm-up phase. These are referred to as microfronts, for example, by Williams and Hacker [5] and Stull [14]. Williams and Hacker [21] describe how surface layer features can be advected into the mixed layer throughout a thermal column and affect the overall structure and dynamics of the thermal column. Hunt [20] describes detrainment effects that mix air from the thermal with the surrounding air leewards of the thermal. Such effects may cause the diffuse characteristics of the courses on the leeward side. Another issue may arise due to the normalization of the thermal diameter which may misrepresent fluctuations and has been discussed by Williams and Hacker [5].

Conclusion and Outlook

A methodology to measure characteristics of thermal updrafts using a miniaturized chilled mirror hygrometer aboard a research glider has been demonstrated. Results on the scalar variables contributing to air density differences, temperature and humidity in particular, are in agreement with existing meteorological literature. The adopted pass-through flight strategy produced

cross-sectional data. Notably, an asymmetric horizontal fine-structure in humidity and temperature profiles within thermal updrafts was measured. Updrafts displayed an elongation approximately twice as long in the main wind direction. However, the dataset is limited in three ways. Due to the small number of samples no trends or values of statistical significance could be derived. Secondly, the data set only covers the upper half of the CBL. Thirdly, there is little information on key factors influencing thermal dynamics such as the flux of heat and latent heat on the ground, wind speed and mixed layer temperature over time. Improvements could be achieved not only by more glider measurements but also by using a powered carrier platform with a similar flight speed and aerodynamic properties such as a motor glider, small motor aircraft or unmanned system. A powered system could provide longer measurement sections for better reference temperatures as well as coverage in the lower part of the atmospheric boundary layer closer to the origin of thermals.

Acknowledgments

The authors would like to thank the Institute of Aerodynamics and Flow Technology and the Flight Experiments department of the German Aerospace Center which provided the necessary infrastructure for the construction and calibration of the FTHP, as well as the Discus-2c DLR as a measurement platform. Many thanks also go to the Environmental Physics Group of the Center for Applied Geoscience at the University of Tübingen for providing the CMH prototype and meteorological evaluation software. Further thanks go to Richard Czuberny for the assistance with designing and building the electronic hardware, Frank Beyrich from the German Meteorological Service (DWD) for providing meteorological data as reference data and Klaus Schäfer for the very helpful input on the control system of the CMH. Finally, we would like to thank Idaflieg for carrying out the flight operations in Stendal and Akaflieg Brauschweig for providing the Duo Discus XL with the MASB measuring system.

References

[1] Norbert Kalthoff, Katja Träumner, Bianca Adler, Stephan Späth, Andreas Behrendt, Andreas Wieser, Jan Handwerker, Fabio Madonna, and Volker Wulfmeyer. Corrigendum: Dry and moist convection in the boundary layer over the Black Forest - a combined analysis of in situ and remote sensing data MetZ. 22, 4. *Meteorologische Zeitschrift*, 22(6):787–788, 2013. doi:10.1127/0941-2948/2013/0556.

[2] C. Kiemle, G. Ehret, A. Fix, M. Wirth, G. Poberaj, W. A. Brewer, R. M. Hardesty, C. Senff, and M. A. LeMone. Latent Heat Flux Profiles from Collocated Airborne Water Vapor and Wind Lidars during IHOP_2002. *Journal of Atmospheric and Oceanic Technology*, 24(4):627–639, 2007. doi:10.1175/JTECH1997.1.

[3] Donald H. Lenschow. *Probing the Atmospheric Boundary Layer*. American Meteorological Society, Boston, MA, 1986. doi:10.1007/978-1-944970-14-7.

[4] Manfred Wendisch, editor. *Airborne measurements for environmental research: Methods and instruments*. Wiley series in atmospheric physics and remote sensing. Wiley-VCH, Weinheim, 2013. doi:10.1002/9783527653218.

[5] A. G. Williams and J. M. Hacker. The composite shape and structure of coherent eddies in the convective boundary layer. *Boundary-Layer Meteorology*, 61(3):213–245, 1992. doi:10.1007/BF02042933.

[6] D. H. Lenschow. Airplane Measurements of Planetary Boundary Layer Structure. *Journal of Applied Meteorology*, 9(6):874–884, 1970. doi:10.1175/1520-0450(1970)009<0874:AMOPBL>2.0.CO;2.

[7] D. Konovalov. On the Structure of Thermals. *Technical Soaring*, 29(4):121–126, 2005. URL: https://journals.sfu.ca/ts/index.php/ts/article/view/206.

[8] Falk Pätzold. *Windmessung mittels Segelflugzeug*, volume 2018, 04 of *Berichte aus der Luft- und Raumfahrttechnik*. TU Braunschweig, Niedersächsisches Forschungszentrum für Luftfahrt, Braunschweig, 2018. doi:10.24355/dbbs.084-201805221102-1.

[9] Oliver Predelli and Ronald Niederhagen. Humidity, the Dominating Force of Thermal Updrafts. *Technical Soaring*, 45(1), 2021. URL: https://journals.sfu.ca/ts/index.php/ts/article/view/2217.

[10] Alfred Ultsch and Christof Maul. Meteorological fine structures of Thermals. OSTIV Met Panel Meeting, 2019. URL: https://ostiv.org/sections/scientific-section/meteorological-panel/met-meetings/met-meeting-2019-frankfurt.html.

[11] Dietrich Sonntag, Thomas Foken, Holger Vömel, and Olaf Hellmuth. Humidity Sensors. In Thomas Foken, editor, *Springer Handbook of Atmospheric Measurements*, pages 209–241. Springer International Publishing, Cham, 2021. doi:10.1007/978-3-030-52171-4.

[12] Astrid Lampert, Jörg Hartmann, Falk Pätzold, Lennart Lobitz, Peter Hecker, Katrin Kohnert, Eric Larmanou, Andrei Serafimovich, and Torsten Sachs. Comparison of Lyman-alpha and LI-COR infrared hygrometers for airborne measurement of turbulent fluctuations of water vapour. *Atmospheric Measurement Techniques*, 11(4):2523–2536, 2018. doi:10.5194/amt-11-2523-2018.

[13] Moritz Mauz, Bram van Kesteren, Wolfgang Junkermann, Kjell zum Berge, Martin Schön, Andreas Platis, and Jens

Bange. Miniature high-frequency chilled-mirror hygrometer for atmospheric measurements aboard fixed wing UAS. *Meteorologische Zeitschrift*, 29(6):439–449, 2020. doi:10.1127/metz/2020/1026.

[14] Roland B. Stull. *An introduction to boundary layer meteorology*. Kluwer Academic Publishers, Dordrecht, 1988. doi:10.1007/978-94-009-3027-8.

[15] Roland B. Stull. *Practical meteorology: An algebra-based survey of atmospheric science*. University of British Columbia, Vancouver, BC, Canada, version 1.02b edition, 2017. URL: https://www.eoas.ubc.ca/books/Practical_Meteorology.

[16] Jens Bange. *Airborne measurement of turbulent energy exchange between the earth surface and the atmosphere*. Habilitation Thesis, 2007. URL: https://www.gbv.de/dms/bs/toc/617124590.pdf.

[17] N. Wildmann, M. Mauz, and J. Bange. Two fast temperature sensors for probing of the atmospheric boundary layer using small remotely piloted aircraft (RPA). *Atmospheric Measurement Techniques*, 6(8):2101–2113, 2013. doi:10.5194/amt-6-2101-2013.

[18] Yann Georg Büchau, Hasan Mashni, Matteo Bramati, Vasileios Savvakis, Ines Schäfer, Saskia Jung, Gabriela Miranda-Garcia, Daniel Hardt, and Jens Bange. PARMESAN: Meteorological Timeseries and Turbulence Analysis Backed by Symbolic Mathematics. doi:10.48550/arXiv.2309.15063.

[19] John Roy Garratt. *The atmospheric boundary layer*. Cambridge atmospheric and space science series. Cambridge University Press, Cambridge, 1. paperback ed. (with corr.) edition, 1999. URL: https://www.cambridge.org/ca/universitypress/subjects/earth-and-environmental-science/atmospheric-science-and-meteorology/atmospheric-boundary-layer.

[20] J. C. R. Hunt. Eddy Dynamics and Kinematics of Convective Turbulence. In E. J. Plate, E. E. Fedorovich, D. X. Viegas, and J. C. Wyngaard, editors, *Buoyant Convection in Geophysical Flows*, pages 41–82. Springer Netherlands, Dordrecht, 1998. doi:10.1007/978-94-011-5058-3_3.

[21] A. G. Williams and J. M. Hacker. Interactions between coherent eddies in the lower convective boundary layer. 64(1-2):55–74. URL: http://link.springer.com/10.1007/BF00705662, doi:10.1007/BF00705662.

[22] Christian Raab and Kai Rohde-Brandenburger. Dynamic flight load measurements with MEMS pressure sensors. *CEAS Aeronautical Journal*, 12(4):737–753, 2021. doi:10.1007/s13272-021-00529-3.

[23] Datasheet SHT3x-DIS, 2022. URL: https://sensirion.com/media/documents/213E6A3B/63A5A569/Datasheet_SHT3x_DIS.pdf.

[24] Kai Rohde-Brandenburger. Berechnung von neuen Handicap-Faktoren für die Wertung von Segelflugzeugen in der Club-Klasse. Institut für Aerodynamik und Strömungstechnik, DLR Braunschweig. doi:10.13140/RG.2.2.15641.80489.

[25] Michael Greiner and Werner Würz. In-flight measurement of free-stream turbulence in the convective boundary layer. *Experiments in Fluids*, 63(10), 2022. doi:10.1007/s00348-022-03506-6.

[26] J. R. Milford. Some Statistics of Thermals Observed by a Powered Sailplane. XVI OSTIV-Congress, 1978. URL: https://journals.sfu.ca/ts/index.php/op/article/view/1864/1785.

[27] Oliver Maas and Dieter Etling. On the influence of moisture on the strength of thermals: A large-eddy simulation case study. *Technical Soaring*, 45(3), 2021. URL: https://journals.sfu.ca/ts/index.php/ts/article/view/2241/2145.

[28] I. S. Bowen. The Ratio of Heat Losses by Conduction and by Evaporation from any Water Surface. 27(6):779–787. URL: https://link.aps.org/doi/10.1103/PhysRev.27.779, doi:10.1103/PhysRev.27.779.

[29] Björn Maronga, Sabine Banzhaf, Cornelia Burmeister, Thomas Esch, Renate Forkel, Dominik Fröhlich, Vladimir Fuka, Katrin Frieda Gehrke, Jan Geletič, Sebastian Giersch, Tobias Gronemeier, Günter Groß, Wieke Heldens, Antti Hellsten, Fabian Hoffmann, Atsushi Inagaki, Eckhard Kadasch, Farah Kanani-Sühring, Klaus Ketelsen, Basit Ali Khan, Christoph Knigge, Helge Knoop, Pavel Krč, Mona Kurppa, Halim Maamari, Andreas Matzarakis, Matthias Mauder, Matthias Pallasch, Dirk Pavlik, Jens Pfafferott, Jaroslav Resler, Sascha Rissmann, Emmanuele Russo, Mohamed Salim, Michael Schrempf, Johannes Schwenkel, Gunther Seckmeyer, Sebastian Schubert, Matthias Sühring, Robert von Tils, Lukas Vollmer, Simon Ward, Björn Witha, Hauke Wurps, Julian Zeidler, and Siegfried Raasch. Overview of the PALM model system 6.0. *Geoscientific Model Development*, 13(3):1335–1372, 2020. doi:10.5194/gmd-13-1335-2020.

[30] Michael Allen. Updraft Model for Development of Autonomous Soaring Uninhabited Air Vehicles. In *Aerospace Sciences Meetings*, 2006. doi:10.2514/6.2006-1510.

[31] Christopher E. Childress. *An Empirical Model of Thermal Updrafts Using Data Obtained From a Manned Glider*. Master Thesis, University of Tennessee, Knoxville, 2010. URL: https://trace.tennessee.edu/utk_gradthes/612/.

[32] D. H. Lenschow and P. L. Stephens. The role of thermals in the convective boundary layer. *Boundary-Layer Meteorology*, 19(4):509–532, 1980. doi:10.1007/BF00122351.

[33] B. H. Carmichel. What Price Performance? *Soaring*, (18):6–10, 1954.

[34] Alfred Ultsch. Swarm Data Mining for the Fine Structure of Thermals. *Technical Soaring*, 36(4):102–111, 2012. URL: https://journals.sfu.ca/ts/index.php/ts/article/view/337.

[35] Krzysztof Kubrynski. Aerodynamic design and cross-country flight performance analysis of Diana-2 sailplane. *Technical Soaring*, (Vol. 30, No. 3):79–88, 2006. URL: https://journals.sfu.ca/ts/index.php/ts/article/view/189/174.

[36] K. Träumner, Th. Damian, Ch. Stawiarski, and A. Wieser. Turbulent Structures and Coherence in the Atmospheric Surface Layer. *Boundary-Layer Meteorology*, 154(1):1–25, 2015. doi:10.1007/s10546-014-9967-6.

[37] Karl-Heinz Horstmann. Neue Modellaufwindverteilungen und ihr Einfluss auf die Auslegung von Segelflugzeugen. XV OSTIV-Congress, 1976. URL: https://journals.sfu.ca/ts/index.php/op/article/view/1793/1714.

[38] Stefan Ronig. *Überarbeitung des Indexsystems für Segelflugzeuge zur Verbesserung der Chancengleichheit auf Wettbewerben mit Flugzeugen unterschiedlicher Leistungsfähigkeit*. Project Thesis, 1995. URL: https://elib.dlr.de/36381/.

[39] Carsten Lindemann. Some characteristics of thermal convection as measured by a powered sailplane. XV OSTIV Crongress, 1976. URL: https://journals.sfu.ca/ts/index.php/op/article/view/1818/1739.

[40] J. R. Milford. Some Thermal Sections Shown by an Instumented Glider. XIII OSTIV-Congress, 1972. URL: https://journals.sfu.ca/ts/index.php/op/article/view/1741/1662.

[41] Carsten Lindemann. The Powered Sailplane as an Instrument Platform for Meteorological Research of the Planetary Boundary Layer and first Measurement Results. XIV OSTIV-Congress,, 1974. URL: https://journals.sfu.ca/ts/index.php/op/article/view/1779/1700.

[42] Roland B. Stull. A Convective Transport Theory for Surface Fluxes. *Journal of the Atmospheric Sciences*, 51(1):3–22, 1994. doi:10.1175/1520-0469(1994)051<0003:ACTTFS>2.0.CO;2.

Appendix

Measurement Flights

Flight 1 The first flight took place in a high-pressure weather situation with good thermals and an exceptionally high cloud base of just under 3 km. Due to airspace C, which begins at 3 km altitude, the aerotow could not be carried out above the CBL. The cloud coverage was $2/8 - 3/8$ cumulus.

After being towed to the upper third of the CBL, measurement sections were flown to validate the measurement system (influence of airspeed and sideslip). These were carried out in the area between the cumulus clouds in order to keep the influence of the updrafts on the validation to a minimum.

After validation, five horizontal thermal cross-sections were flown in three updrafts, each with a headwind and a crosswind section.

Flight 2 The second flight was a tow transfer flight below the cloud base from Braunschweig to Stendal. After the passage of a cold front in the previous night, good thermals developed with a cloud coverage of around $4/8$. After the transfer, six horizontal thermal cross-sections, each with a headwind and a crosswind section, were flown in five updrafts.

Flight 3 The third flight took place in the late afternoon on a day with moderate cloud thermals and $2/8 - 3/8$ coverage. It was started in aerotow up to above the cloud tops. After that, two long straight measurement sections were carried out up to below the cloud base with $100\,\mathrm{km\,h^{-1}}$ IAS to validate the new CMH firmware. After that, four more horizontal thermal cross-sections were then carried out in one thermal, two headwind and two tailwind sections.

Table 1: Summarized data of the measurement flights.

Flight no.	1	2	3
Date	04.08.2022	06.08.2022	25.08.2022
Departure Location	Brunswick	Brunswick	Stendal
Arrival Location	Brunswick	Stendal	Stendal
Departure Time (LT)	14:34	11:46	16:38
Arrival Time (LT)	17:21	13:52	18:09
Flight duration	2:38	2:08	1:55
Cloud base [m]	2800	1500	1200
Wind direction [°]	200	330	80
Wind speed [m/s]	6	4	5
Barometric pressure at MSL [hPa]	1002	1013	1005
z_i [m]	3200	1800	1300
$\overline{\Theta}$ [°C]	34.9	17.0	26.4
$\overline{\Theta_v}$ [°C]	36.3	18.0	28.6